Optics & Laser Technology 91 (2017) 1–6

Contents lists available at ScienceDirect

Optics & Laser Technology

journal homepage: www.elsevier.com/locate/optlastec

Full length article

CW and passively Q-Switched operation of a Ho:YAG waveguide laser

Sean A. McDaniel[a,b,*], Patrick A. Berry[a], Gary Cook[a], David Zelmon[a], Stephanie Meissner[c], Helmuth Meissner[c], Xaiodong Mu[c]

[a] Air Force Research Laboratory, Sensors Directorate, 2241 Avionics Circle, Wright-Patterson AFB, OH 45433, USA
[b] Leidos Inc., 3745 Pentagon Blvd, Beavercreek, OH 45431, USA
[c] Onyx Optics Inc., 6551 Sierra Lane, Dublin, CA 94568, USA

ARTICLE INFO

Keywords:
Solid-state lasers
Infrared lasers
Channeled waveguides
Ho:YAG

ABSTRACT

We report the first demonstration of a Ho: YAG crystal fiber waveguide (CFW) laser operating at 2.09 μm. The CFW structure was produced by adhesive free bonding of holmium doped yttrium aluminum garnet core to an undoped yttrium aluminum garnet cladding. The laser produced CW output powers greater than 500 mW with slope efficiency of 17%. The same crystal when passively Q-switched with Cr: ZnSe, produced pulsed output with energies of 1 μJ at a repetition frequency of 442 kHz.

1. Introduction

In recent years, 2 μm laser sources have seen a growth in utility. Lasers that operate in the 2 μm range, most notably Ho:YAG and Tm:YAG, are considered eye-safe due to the high absorption of light in eye tissue and intraocular fluid. Eye-safe operation, along with several organic absorption lines, drive the need for advancement of 2 μm laser sources, to enable compact, high power systems capable of CW and Q-Switched operation. In this work, we demonstrate the use of Ho:YAG CFW structures to demonstrate a compact laser source, which could be suitable for such applications.

Ho:YAG lasers operating in the 2 μm range have numerous applications including medical [1], dental [2] and as optical pump sources for other laser materials [3–5]. Ho:YAG can easily be pumped by 1.9 μm radiation, usually from a thulium fiber laser [6] or from cross relaxation of a thulium ion under diode pumping at 780 nm in a co-doped crystal. The laser operates on the holmium $^5I_7$-$^5I_8$ [7] transition producing 2.09 μm radiation. This transition has been shown to be active at room temperature [8] and capable of producing high power output.

One approach to guided-wave operation of Ho:YAG laser would be through doping of crystalline YAG fibers [9]. However, high losses in these fibers have so far prevented them from being a viable option for passive or active devices. A more popularized approach is holmium doping of ZBLAN fibers [10,11] or co-doping of holmium and thulium in ZBLAN fibers [12,13]. A maximum output of 6.6 W has been obtained from a Ho:ZBLAN fiber [14]. Additionally, Tm, Ho and co-doped Tm Ho silica fibers have been created with output powers in excess of 80 W [15–19] and are commercially available from vendors including IPG Photonics and NuFern. Direct creation of waveguides in bulk material using ultrafast laser inscription is an approach that was successfully used in YAG [20] and has produced waveguide lasers in Tm:YAG [21]. An alternative approach to guided wave structures using holmium can be realized by adhesive-free bonding (AFB) of a doped YAG core inside of a undoped YAG substrate. This was first used to demonstrate planar waveguides in Tm:YAG but has only recently been successfully demonstrated in a double-clad, fully confined CFW device with Er:YAG [22].

In this paper, we will present the first demonstration of a Ho:YAG CFW laser. Waveguide operation of this material allows for several advantages over bulk operation including improved longitudinal overlap between pump and laser mode, reduced system complexity and increased thermal management properties due to the small active region size and high thermal conductivity of YAG (0.14 $Wcm^{-1}K^{-1}$) [23].

2. Crystal fiber waveguide construction

The CFW was made from high optical quality single crystal 2 *at.*% Ho:YAG with Onyx Optics adhesive-free bonding technology (AFB). In order to form the desired fiber core size with an undoped YAG cladding, multiple bonding processes with precision milling and polishing processes were applied. Since the trivalent Ho^{3+} ion in YAG occupied the Y^{3+} lattice position that surround by eight oxygen ions, ion diffusion from the Ho:YAG to the un-doped YAG can rarely happen in the CFW fabrication process. The waveguide can be considered to have a perfect step-index profile. The refractive index difference is

* Corresponding author at: Leidos Inc., 3745 Pentagon Blvd, Beavercreek, OH 45431, USA.
E-mail address: sean.a.mcdaniel@leidos.com (S.A. McDaniel).

http://dx.doi.org/10.1016/j.optlastec.2016.12.004
Received 30 June 2016; Accepted 8 December 2016
Available online 16 December 2016
0030-3992/

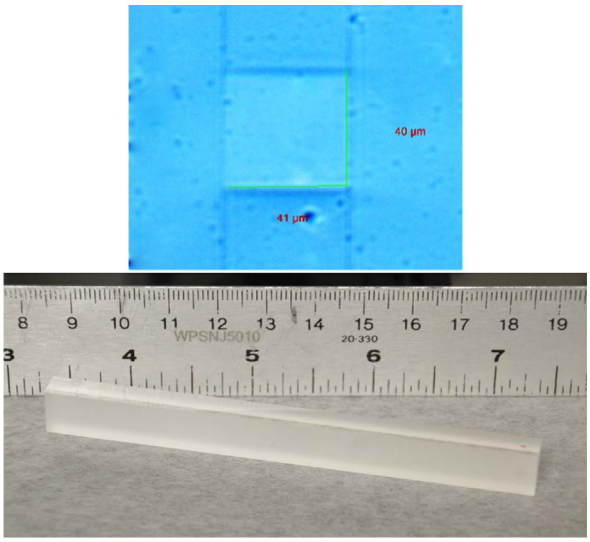

Fig. 1. Ho:YAG waveguide 40 × 40 μm core surrounded by undoped YAG.

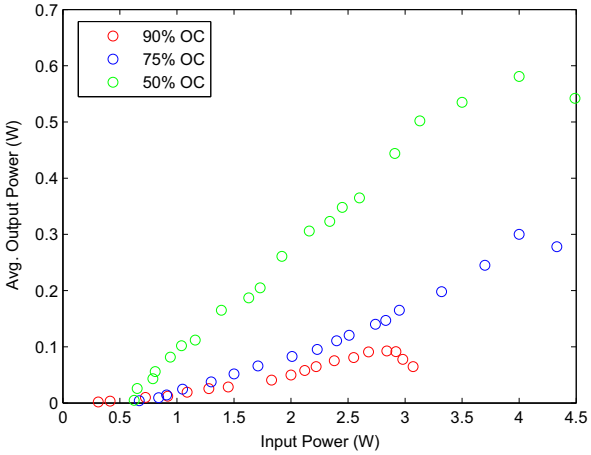

Fig. 3. Waveguide Ho:YAG slope efficiency for 90%, 75% and 50% reflective outcouplers. The output power presented in this graph represents average power on a thermopile power meter.

around 4.88×10^{-4} as measured by an interferometric method at wavelength of 1.55 μm [24]. The corresponding numerical aperture (NA) was 0.042. We have assumed that the index difference in the core of the waveguide only arises from the inclusion of the holmium dopant. The material dispersion relation in the region of 1.55 – 2 μm is relatively constant, thus the NA of the waveguide at 1.55 μm provides a good estimation of the NA at 2.1 μm.

3. CW experimental setup

The Ho:YAG waveguide consisted of a 40 × 40 μm doped, square core surrounded by undoped YAG, see Fig. 1. The Ho:YAG core of the waveguide was doped to 2 at% and was 100 mm long. The total dimensions of the waveguide crystal were 84 mm×9.8 mm×6.2 mm ($L \times W \times H$). The waveguide was placed on an uncooled mount capable of pitch, yaw and transverse adjustment. We measured the losses of the waveguide using a non-destructive technique, which relies on imaging the scattered light from core of the waveguide [25]. Fitting the scattered light to an exponential provides an upper estimate of the waveguide losses, which were estimated to be 1 dB/cm at 1 μm.

At each end facet of the crystal, flat mirrors were placed to produce a laser cavity. The setup of the waveguide laser can be seen in Fig. 2. This consisted of an isolator (polarizing beam splitter (PBS) and λ/4 waveplate), a 2.5 cm focal length lens with an NA of 0.16 (L1), a dichroic mirror (M1, highly reflective (HR)@2.1 μm and anti-reflective (AR)@1.9 μm), a variable percentage outcoupler for 2.1 μm (M2), a 2.5 cm focal length collimating lens (L2), and a dichroic beam splitter (DI, HR@2.1 μm and AR@1.9 μm at a 45° angle of incidence). The pump source was an IPG thulium fiber laser (Model TLR-20–1908-LP), which produced a pump spot size of 50 μm. The crystal faces were uncoated, producing a Fresnel reflection of approximately 8%. As a precaution to reduce back reflections into the thulium fiber pump laser, index matching gel was used to decrease the Fresnel reflection. Additionally, the polarizing beam cube and a λ/4 waveplate were used as an optical isolator.

Fig. 2. Waveguide setup of the Ho:YAG waveguide structure.

4. CW results

CW operation of the laser was characterized with 90%, 75% and 50% reflective outcouplers (see Fig. 3). It should be noted that all data was taken while the pump beam was chopped at 20 Hz with a 50% duty cycle in order to decrease the thermal load on the Ho:YAG crystal. The best performing outcoupler, 50% reflective, achieved a slope efficiency of 17% and a threshold of 597 mW. The 75% outcoupler had a slope efficiency of 8% and a threshold of 377 mW. Finally, the 90% outcoupler had a slope efficiency of 1.6% and a threshold of 291 mW.

The non-optimal performance can be attributed to several factors. First, the waveguide laser was uncooled. It has been shown by Barnes et al. [27] that as the temperature increases, laser efficiency decreases in Ho:YAG. The thermal properties of YAG are well characterized, thus using standard thermal transport equations the temperature inside of the waveguide can be modeled using COMSOL(TM). The waveguide structure was modeled as a 40 μm square core located several millimeters away from each face of the CFW. A Gaussian beam with diameter 50 μm was modeled to be incident on the core of the CFW. Using Beer's law absorption, the heat deposition profile was modeled in the waveguide structure. The core of the waveguide had a doping concentration of 2 at%, with an absorption cross section of 1.2×10^{20} cm^2 at 1908 nm. The model calculated a rise in temperature of approximately 52 K for 5 W of incident pump power. From the generated temperature profile, Fig. 4, a parabolic profile was fitted to the temperature gradient. The parabolic profile from Koechner and Bass [28](Eq. (1)) was then used, neglecting stress-dependent variations, to calculated the effective change in index due to the thermal load on the waveguide assuming an absorption depth of 2 cm, see Fig. 5. In Eq. (1), n_0 was the unmodified index, $T(r)$ was the radially dependent temperature, $T(0)$ was the initial temperature and $\frac{dn}{dT}$ was the thermo-optic coefficient for YAG(7.8×10^{-6} K^{-1}).

$$n(r) = n_0 + (T(r) - T(0))\frac{dn}{dT} \quad (1)$$

From Fig. 5, it can be seen that the temperature dependent index profile was approximately flat across the core of the waveguide. From the temperature dependent index profile, beam propagation method (BPM) can be used to test the stability of the waveguide under normal operating conditions, Fig. 6. For the conditions listed in this paper, the propagating mode does not experience significant thermal lensing due to the heat load on the waveguide. Additionally, if the stress-dependent variation in material index was present in the waveguide, an increase in the effective focal length of the material on the order of 20% can be

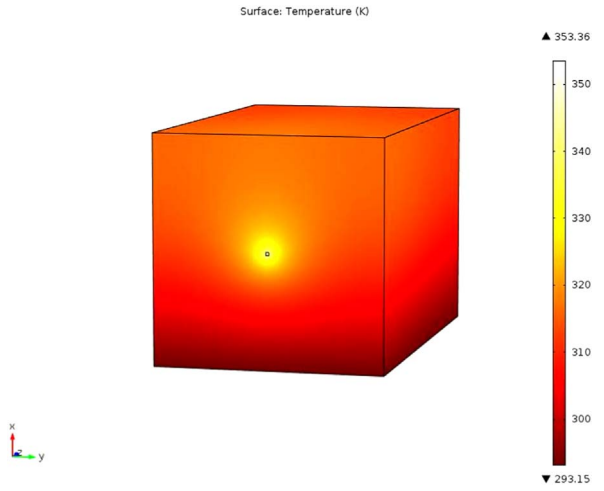

Fig. 4. Modeled heat distribution inside of the Ho: YAG waveguide structure. The figure shows a 2 mm×2 mm section of the waveguide.

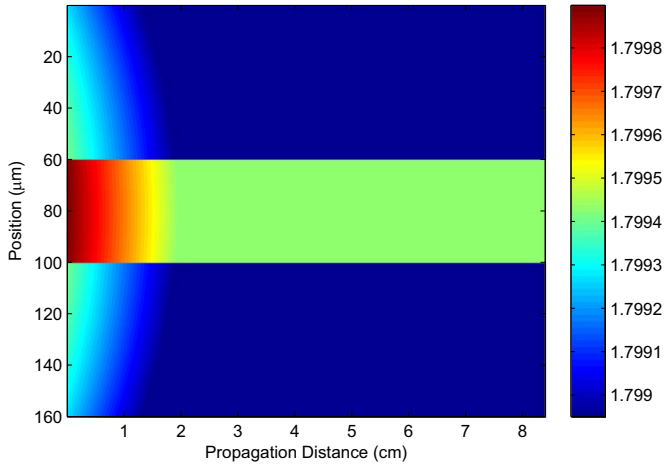

Fig. 5. Modified index profile accounting for the thermally induced index change in the waveguide. The direction of propagation is from left to right.

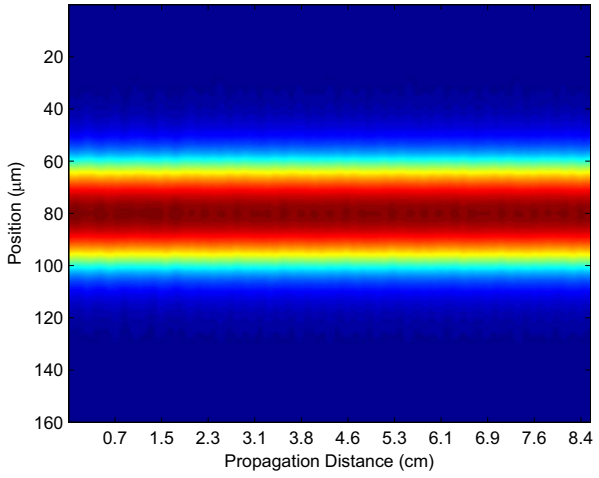

Fig. 6. Propagated mode using the BPM technique assuming the refractive index profile shown in Fig. 5. The graph shows the scaled field propagating perpendicular to the direction of propagation.

expected [29]. The additional change in refractive index due to the material stress does not affect the propagating mode significantly.

Second, reabsorption of the emitted light from CFW laser will contribute to an increased threshold, which means that higher pump powers will be needed to reach threshold. Increased pump power will increase the temperature of the waveguide, decreasing the laser efficiency. If an absorption coefficient of 2 cm^{-1} is assumed, which is approximately the absorption coefficient of 2 at% doped Ho:YAG, this produces 95% absorption of the pump light at 1.5 cm leaving the additional 6.9 cm to absorb the emitted light. Additionally, the mode structure of the waveguide can be investigated. The confined mode field of the laser can be numerically calculated using Eq. (2), which was formulated using a finite difference formulation of the 1-D Maxwell wave equation for TE modes. In Eq. (2), k_0 was $\frac{2\pi}{\lambda}$, n was the refractive index profile of the waveguide, E was the normalized electric field, Δx was the calculation step size and n_{eff} was the estimated effective index. Eq. (2) was iteratively solved using a differential minimization technique. These index difference was in the range of $\Delta n \approx 0.00048$ producing numerical apertures of 0.042. The index difference was measured using an interferometric, phase delay method across the interface of undoped and doped material. From the presented measurment of Δn, we would expect a confinement factor of approximately 95%.

$$E(x + \Delta x) = (2 - k_0^2 * (n(x)^2 - n_{eff}^2) * \Delta x^2) * E(x) - E(x - \Delta x) \quad (2)$$

Eq. (2) can also be used to estimate the output mode of the laser. Combining two solutions for the vertical and horizontal directions, the mode structure in Fig. 7 was obtained. From Fig. 7, it can be seen that the supported mode size of the laser was 58 μm ($\frac{1}{e^2}$ diameter) using an

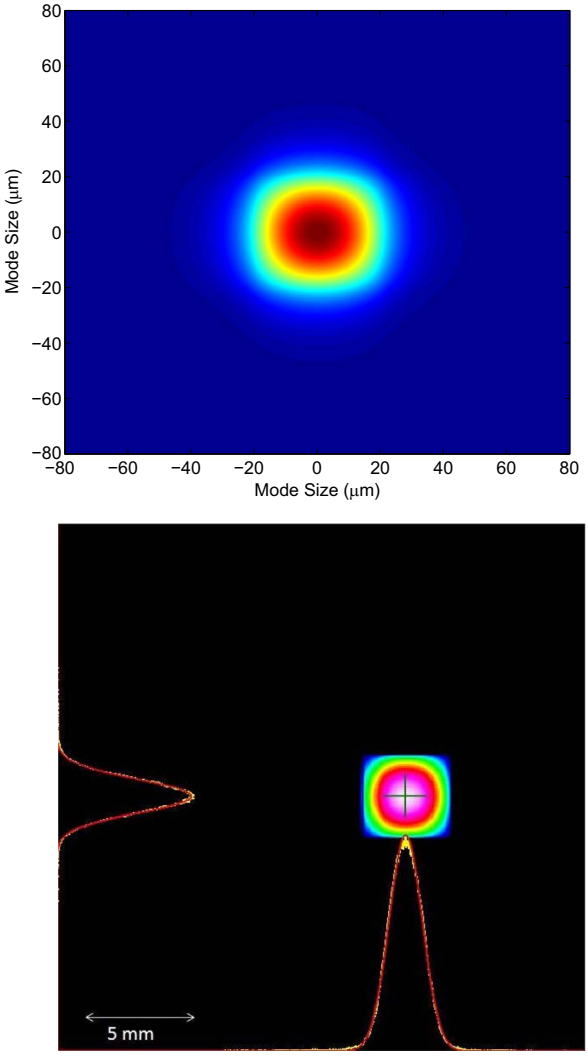

Fig. 7. (Upper)Normalized near field guided mode structure of the Ho: YAG waveguide calculated from Eq. (2). (Lower) Output mode measured by a ThorLabs BP109-IR2 beam profilier at a distance of 10 cm from the waveguide.

NA of 0.042. The mode size can then be calculated at a distance of 10 cm by using the angular spread associated with the measured NA. At a distance of 10 cm, a beam size of 4.2 mm was calculated, which was approximately the actual beam size shown in Fig. 7. The beam exhibited TEM_{00} operation. For a square core fiber, the nature of the confined mode fields for dielectric rectangular waveguides has been discussed by many authors [30–33]. The small difference between the refractive index of the guide and those of the surrounding regions permits the separate solution for the propagation constants for the x and y directions. If we assume that the electric field varies as $e^{-i\beta z}$, we can solve the wave equation in the cladding and core regions by applying the boundary conditions. The tangential components of E and H are continuous across the boundaries between the core and the cladding and exponentially vanishing solutions outside the cladding were used to calculate the propagation constants in all regions. From these solutions, one may calculate the field distributions and mode structure in an arbitrary waveguide structure. Since all of the cladding materials are identical, the expressions for the transverse propagation constants k_x and k_y are given below.

$$k_x a = p\pi - 2\tan^{-1} k_x \xi \tag{3}$$

$$k_y a = q\pi - 2\tan^{-1} \frac{n_{cl}^2}{n_g^2} k_y \eta \tag{4}$$

In the above equations, $\xi = \frac{1}{\sqrt{k_g^2 - k_{cl}^2 - k_x^2}}$, $\eta = \frac{1}{\sqrt{k_g^2 - k_{cl}^2 - k_y^2}}$, n_g was the guide refractive index and n_{cl} was the cladding refractive index. Additionally, p and q are integers indicating the mode index. We have solved these equations numerically and found that if the difference in refractive index between the core and the cladding was 0.00048 [24], for a 40 μm × 40 μm cross section waveguide, only a single waveguide mode exists. The mode, E_{11}, has propagation constants $k_x = 0.0084984\ \mu m^{-1}$ and $k_y = 0.0084965\ \mu m^{-1}$.

The output spectrum of each outcoupler, near the maximum output power, was coupled into a fiber coupled optical spectrum analyzer(OSA). The Yokogawa AQ6375 OSA had a spectral resolution of 0.01 nm. The normalized output spectra can be seen in Fig. 8. All outputs were centered around 2097 nm with spectral widths of approximately 0.5 nm.

5. Q-switched setup

While CW operation is useful for some applications, other, such as medical and dental, require peak powers associated with pulsed operation. Ho:YAG has a long upper-state lifetime which lends itself to Q-switching, either actively [3] or passively using materials such as Cr:ZnSe [26]. The waveguide setup was modified to accept a passive Q-

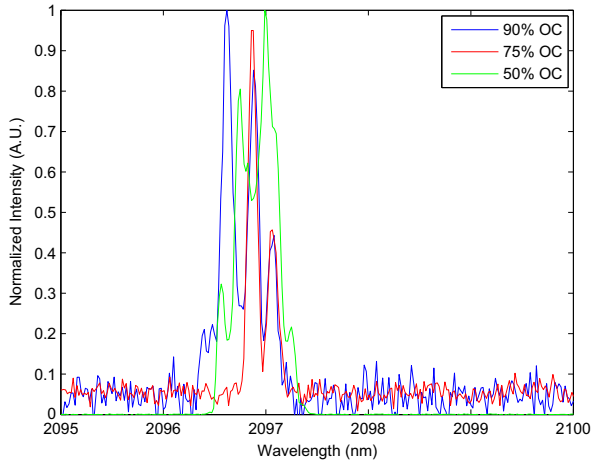

Fig. 8. Normalized emission spectra for 90%, 75% and 50% reflective outcouplers.

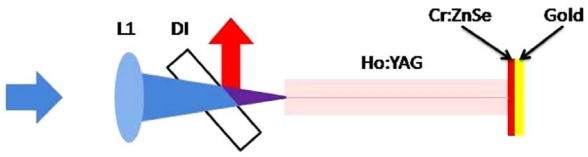

Fig. 9. Experimental setup of the Q-switched Ho: YAG waveguide laser.

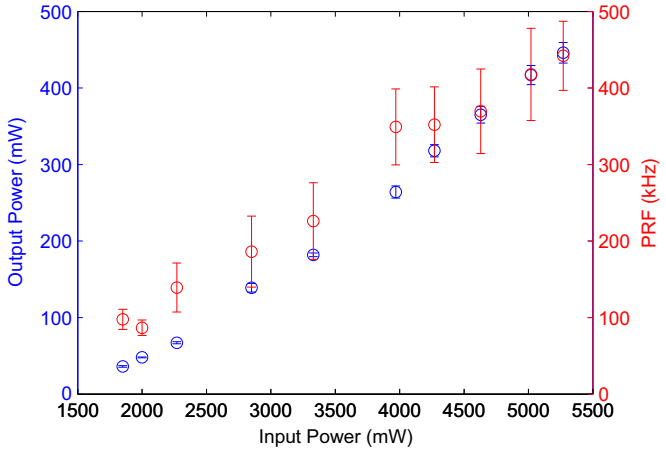

Fig. 10. Output power measurements and PRF measurements of the Q-switched waveguide laser.

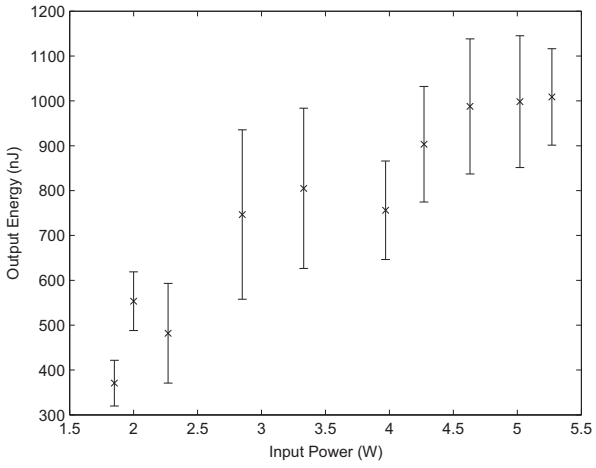

Fig. 11. Output pulse measurement as a function of input power. The errorbars represent the differential error analysis dependent on the standard deviation of the output power and PRF.

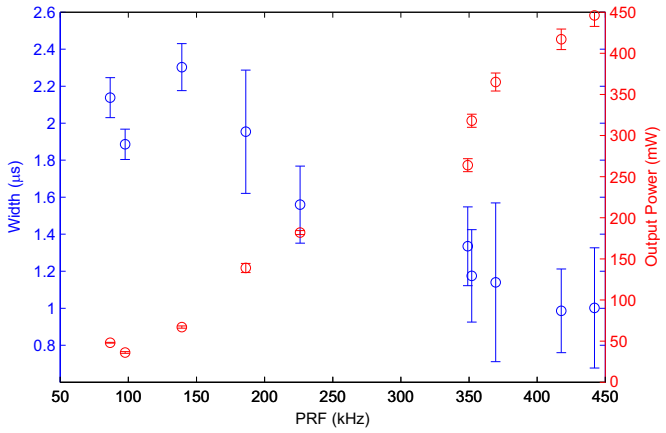

Fig. 12. Output power measurements and Pulse width measurements of the Q-switched waveguide laser as a function of PRF.

switch, see Fig. 9. The passive Q-switch was a thin-disk Cr:ZnSe sample, which was 250 μm thick and doped to 1×10^{19} cm^{-3}. The thin disk was AR coated on the front and HR gold coated on the back. The setup shown in Fig. 9 relies on Fresnel reflection to act as an outcoupler. Fresnel reflection for YAG was approximately 8% using the index from Zelmon et al. [34].

6. Q-switched results

Adjusting input power produced pulsed operation of the waveguide (Fig. 10). The output wavelength of the laser shifted from 2097 nm to 2091 nm, but the output mode remained unchanged. From Fig. 10, it can be seen that as the output power increases, so does the PRF(pulse repetition frequency). The PRF is related to the output power and saturation time of the passive Q-switch. As the input power was increased, the output power increases saturating the passive Q-switch faster. Thus, in order to get increased power out of the system, the PRF needs to increase.

Knowing the output power and repetition rate, we can convert the average power into an average pulse energy, see Fig. 11. The error bars in Fig. 11 were calculated using differential error analysis of the PRF and fluctuations in the output power. Using a LeCroy WaveRunner oscilloscope and an extended range InGaAs detector, the Ho:YAG laser pulses were observed. Utilizing the pulse statistics, the standard deviation of the pulse energy was calculated. From Fig. 11, it can be seen that the error bars are large due to the large variation in the PRF of the laser. However, average pulse energies of greater than 1 μJ were obtained.

Additionally, it was observed that as the PRF increases, the pulse width decreases (Fig. 12). This is likely due to stronger signal present at higher repetition rates. In other words, the faster the saturable absorber is bleached, the faster the gain media can emit its stored energy. It should be noted that the long pulse width, on the order of 2 μs was not expected from the setup. However, it can be easily explained by noting when the saturable absorber becomes transparent (i.e. when saturation intensity is reached). It can be seen that the saturation intensity, Eq. (5), is inversely related to the lifetime of the absorbing material (τ). In this case, the absorbing material was Cr:ZnSe, which has a upper state lifetime of 5 – 7 μs [35]. Thus, depending on losses due to the saturable absorber and the spot size on the absorber, the saturation intensity can be large. Assuming a lasing wavelength of 2097 nm, total cross section(σ) of approximately 1×10^{-20} cm^2 and a spot size of 58 μm, the saturation power can be on the order of several hundred mW. Coupling a large saturation power with a weak laser signal, similar to what was observed at low PRF with this system, can lead to long pulse widths.

$$I_{sat} = \frac{h\nu}{\sigma\tau} \tag{5}$$

Likewise, a good approximation of Q-switched pulse widths is given by Siegman [36], Eq. (6), which shows that the pulse width is approximately dependent on the inversion ratio, r, the energy extraction efficiency, η, and the cavity lifetime, τ_c. Assuming an inversion ratio near unity, which is valid for near threshold conditions, and a cavity lifetime which was calculated from $\tau_c = -\frac{2L}{c * \ln(R_1 R_2)}$, where R_1 and R_2 are the mirror reflectivities and L is the length of the system, pulses on the order of microseconds can be expected.

$$\tau_p \approx \frac{r\eta(r)}{r - 1 - \ln(r)} \times \tau_c \tag{6}$$

The theory shown in Eq. (6) predicts a pulse width of 3 μs for an inversion ration of near unity and mirror reflectivities of 8% and 94%. Approximate unity inversion ratio is assumed for near threshold operation. Experimentally, we obtained 2.2 μs pulses for operation slightly above threshold. At near theshold pumping conditions, the pulse rate and pulse width was erratic so exact experimental values are not presented due to this inconsistent behavior.

7. Conclusion

In conclusion, we have demonstrated the first ever Ho:YAG CFW laser. This initial demonstrator laser was capable of producing up to 540 mW of CW output using a 50% reflective outcoupler at a laser wavelength of 2097 nm. Adjusting the laser configuration, the same laser sample used for CW testing also produced Q-switched output. The Q-switched configuration employed a Cr:ZnSe passive Q-switch and was exhibited output pulse energies of 1 μJ at a PRF of 442 kHz. Future works will include more efficient laser configurations, such as dual end pumping and different doping concentrations. This work was funded by the U.S. Air Force's Materials and Manufacturing Directorate (contract FA8650-11-D-5401) and Sensors directorate (contract FA8650-12-D-1377).

References

[1] K. Trauner, N. Nishioka, D. Patel, Pulsed holmium yttrium-aluminum-garnet (Ho:YAG) laser ablation of fibrocartilage and articular cartilage, Am. J. Sports Med. 18 (3) (1990) 316–320.
[2] I. Cernavin, A comparison of the effects of Nd:YAG and Ho:YAG laser irradiation on dentine and enamel, Aust. Dent. J. 40 (1995) 79–84.
[3] E. Lippert, S. Nicolas, G. Arisholm, K. Stenersen, G. Rustad, Mid-infrared laser source with high power and beam quality, Appl. Opt. 45 (2006) 3839–3845.
[4] S.A. McDaniel, P.A. Berry, K.L. Schepler, Gain-switched single-pass Cr: ZnSe amplifier, Proc. SPIE 8599 (2013).
[5] H. Cankaya, N. Cizmeciyan, E. Beyath, A. Gorgulu, A. Kurt, A. Sennaroglu, Injection-seeded, gain-switched tunable Cr: ZnSe laser, Opt. Lett. 37 (2012).
[6] D.Y. Shen, et al., Efficient Ho: YAG laser pumped by a cladding-pumped tunable Tm silica-fibre laser, Appl. Phys. B 79 (5) (2004) 559–561.
[7] M. Malinowski, Z. Frukacz, M. Szuflinska, A. Wnuk, M. Kaczkan, Optical transitions of Ho^{3+} in YAG, Journ. Alloy. Compd. 300–301 (2000) 389–394.
[8] R.L. Remski, D.J. Smith, Temperature dependence of pulsed laser threshold in YAG: er^{3+}, Tm^{3+}, Ho^{3+}, J. Quantum Electron. 6 (1970) 750–751 QE.
[9] H.J. Kim, G.E. Fair, S.A. Potticary, M.J. O'Malley, N.G. Usechak, Processing and characterization of polycrystalline YAG (Yttrium Aluminum Garnet) core-clad fibers, Proc. SPIE (2014).
[10] M.C. Brierley, P.W. France, C.A. Miller, Lasing at 2.08 μm and 1.38 μm in a holmium doped fluorozirconate fiber laser, Electron. Lett. 24 (9) (1988) 539–540.
[11] T. Sumiyoshi, H. Sekita, T. Arai, S. Sato, M. Ishihara, M. Kikuchi, High-power continuous-wave 3-mu m and 2-mu m cascade Ho^{3+} ZBLAN fiber laser and its medical applications, IEEE J. Sel. Top. Quantum Electron. 5 (4) (1999) 936–943.
[12] J.Y. Allain, M. Monerie, H. Poignant, High-efficiency CW thulium-sensitised holmium-doped fluoride fibre laser operating at 2.04 mu m, Electron. Lett. 27 (17) (1991) 1513–1515.
[13] R.M. Percival, D. Szebesta, S.T. Davey, N.A. Swain, T.A. King, High-efficiency CW operation of 890 nm pumped holmium fluoride fibre laser, Electron. Lett. 28 (1992) 2064–2066.
[14] A. Guhur, S. Jackson, Efficient holmium-doped fluoride fiber laser emitting 2.1 mu m and blue upconversion fluorescence upon excitation at 2 mu m, Opt. Express 18 (2010) 20164–20169.
[15] W.A. Clarkson, N.P. Barnes, P.W. Turner, J. Nilsson, D.C. Hanna, High-power cladding-pumped Tm-doped silica fiber laser with wavelength tuning from 1860 to 2090 nm, Opt. Lett. 27 (2002) 1989–1991.
[16] S.D. Jackson, F. Bugge, G. Erbert, High-power and highly efficient diode-cladding-pumped Ho^{3+}-doped silica fiber lasers, Opt. Lett. 32 (2007) 3349–3351.
[17] Stuart D. Jackson, Alex Sabella, Alex Hemming, Shayne Bennetts, David G. Lancaster, High-power 83 W holmium-doped silica fiber laser operating with high beam quality, Opt. Lett. 32 (2007) 241–243.
[18] K. Oh, T. Morse, P. Weber, A. Kilian, L. Reinhart, Continuous-wave oscillation of thulium-sensitized holmium-doped silica fiber laser, Opt. Lett. 19 (1994) 278–280.
[19] Florian Jansen, Fabian Stutzki, Cesar Jauregui, Jens Limpert, Andreas Tnnermann, High-power very large mode-area thulium-doped fiber laser, Opt. Lett. 37 (2012) 4546–4548.
[20] A. Rodenas, A. Benayas, J. Macdonald, J. Zhang, D. Tang, D. Jaque, A. Kar, Direct laser writing of near-IR step-index buried channel waveguides in rare earth doped YAG, Opt. Lett. 36 (2011) 3395–3397.
[21] Y. Ren, G. Brown, A. Ródenas, S. Beecher, F. Chen, A. Kar, Mid-infrared waveguide lasers in rare-earth-doped YAG, Opt. Lett. 37 (2012) 3339–3341.
[22] N. Ter-Gabrielyan, V. Fromzel, X. Mu, H. Meissner, M. Dubinskii, High efficiency, resonantly diode pumped, double-clad, Er: YAG-core, waveguide laser, Opt. Express 20 (2012) 25554–25561.
[23] P.H. Klein, W.J. Croft, Thermal conductivity, diffusivity, and expansion of Y_2O_3, $Y_3Al_5O_{12}$, and LaF_3 in the range of 77°–300°K, Appl. Phys. 38 (1967) 1603–1607.
[24] X. Mu, H. Meissner, H.C. Lee, M. Dubinskii, True crystalline fibers double-clad LMA design concept of Tm:YAG-core fiber and mode simulation, Proc. SPIE 8237 (2012) (82373M).
[25] Y. Okamura, S. Yoshinaka, S. Yamamoto, Measuring mode propagation losses of integrated optical waveguides a simple method, Appl. Opt. 22 (1983) 3892–3894.

[26] Y. Terekhov, I.S. Moskalev, D.V. Martyshkin, V.V. Fedorov, S.B. Mirov, Cr-ZnSe passively Q-switched fiber-bulk Ho:YAG hybrid laser, in: Proceedings of the SPIE 7578, Solid State Lasers XIX: Technology and Devices, 75781J (February 17, 2010).
[27] N.P. Barnes, D.J. Gettemy, Performance of Ho: yag as a function of temperature, Appl. Opt. 29 (1990) 404–409.
[28] W. Koechner, M. Bass, Solid-State Laser Engineering, New York, 2006.
[29] W. Koechner, Thermal lensing in a Nd: YAG laser rod, Appl. Opt. 9 (1970) 2548–2553.
[30] G.B. Hocker, W.K. Burns, Mode dispersion in diffused channel waveguides by the effective index method, Appl. Opt. 16 (1976) 113–118.
[31] K. Ogusu, Numerical analysis of the rectangular dielectric waveguide and its modifications, IEEE Trans. Microw. Theory Tech. 25 (1977) 874–885 MTT.
[32] E.A.J. Marcatili, Dielectric rectangular waveguide and directional coupler for integrated optics, Bell Syst. Tech. J. 48 (1969) 2071–2102.
[33] K.S. Chiang, Dual effective-index method for the analysis of rectangular dielectric waveguides, Appl. Opt. 25 (1986) 2169–2174.
[34] D.E. Zelmon, D.L. Small, R. Page, Refractive-index measurements of undoped yttrium aluminum garnet from 0.4 to 5.0 μm, Appl. Opt. 37 (1998) 4933–4935.
[35] I.T. Sorokina, Cr^{2+}-doped II-IV materials for lasers and nonlinear optics, Opt. Mater. 26 (2004) 395–412.
[36] Anthony Siegman, Lasers, Mill Valley, California, 1986.